FULL PAPER

Helium plasma jet interactions with water in well plates

Soheila Mohades[1] | Amanda M. Lietz[2] | Juliusz Kruszelnicki[2] | Mark J. Kushner[1]

[1]Department of Electrical Engineering and Computer Science, University of Michigan, Ann Arbor, Michigan

[2]Department of Nuclear Engineering and Radiological Sciences, University of Michigan, Ann Arbor, Michigan

Correspondence
Mark J. Kushner, Department of Electrical Engineering and Computer Science, University of Michigan, 1301 Beal Ave., Ann Arbor, MI 48109-2122.
Email: mjkush@umich.edu

Present address
Amanda M. Lietz, Sandia National Laboratories, Albuqurque, NM 87185-1423.

Abstract

Plasma activation of liquids or cell cultures is a method for investigating the consequences of plasma produced reactive oxygen and nitrogen species (RONS) on living systems. The reproducible transfer of RONS, ions, electrons, and photons to the liquid is critical for determining reaction mechanisms and biological outcomes, and depends strongly on system parameters. A common in vitro method of plasma treatment of cells is a plasma jet directed into a well plate filled (or partially filled) with a liquid cell growth media. This method of treatment intrinsically has several environmental and geometrical factors that could lead to variability in the activation of the media. Uncontrolled or unreported geometrical and environmental factors that affect this transfer can, therefore, influence the reproducibility of measurements. In this paper, results from a numerical modeling investigation of a pulsed helium plasma jet interacting with water in a well plate are discussed while varying the height of the well-plate rim. The height of the rim changes gas flow patterns, the ratio of He-to-air, and the water vapor content in the gas layer above the liquid. With a low rim, gas flowing from the jet stagnates on-axis and flows radially outward with few vortices that recirculate reactants. With high rims, the gas flow is dominated by vortices and recirculation. With a low rim, the ionization wave (IW) from the jet strikes the liquid and proceeds as a surface IW across the water. With higher rims, the densities of helium and water vapor are higher above the liquid, which results in a volumetric propagation of the IW, initially producing higher densities of H_2, HO_2, OH, and H_2O_2. The end result is that for otherwise identical conditions, the densities of solvated H_2O_{2aq} and select reactive nitrogen species increase with rim height due to the vortices that recirculate reactants.
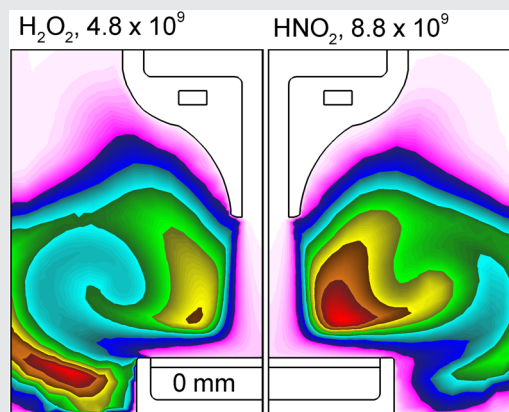
KEYWORDS
atmospheric pressure plasma jet, biotechnology, modeling and simulation, plasma activated liquid

1 | INTRODUCTION

There is increasing interest in the biomedical applications of atmospheric pressure low-temperature plasmas (LTPs) for cancer treatment and bacterial disinfection. For example, rare gas plasma jets interacting with ambient air can produce a significant fluence of reactive oxygen and nitrogen species (RONS) to biological surfaces, such as ozone (O_3) and hydrogen peroxide (H_2O_2), and radicals such as hydroxyl (OH) and nitric oxide (NO). In vitro experiments[1–3] and in vivo studies[4–8] indicate that LTP exposure can induce death in cancer cells,[9,10] suppress cancer cell proliferation,[11,12] and kill bacteria.[13,14] The interaction of plasma with cells may result in the oxidation of macromolecules and proteins, peroxidation of lipids, and damage to DNA which eventually interrupts cell signaling and metabolic processes.[15,16] The RONS produced by LTPs can increase the cells' oxidative stress leading to growth inhibition or cell death.[17–19]

Many investigations have shown that there is a correlation between plasma produced RONS levels and cytotoxic effects. Kurake et al.[20] quantitatively measured H_2O_2 and nitrite (NO_2^-) in plasma-activated media (PAM). They reported on the synergy of H_2O_2 and NO_2^- on killing cancer cells with PAM in which the antitumor effect is not observed when H_2O_2 and NO_2^- are separately applied.[20] In an argon plasma jet in contact with liquid, Kondeti et al.[21] showed that short-lived species such as OH and superoxide (O_2^-) are involved in the inactivation of bacteria in saline solution.

Direct exposure to the gas plasma and the use of PAM are two methods used to transfer RONS to cells and tissues. With the recent attention on PAM, the study of plasma–liquid interactions and the transport of RONS from the gas phase to the liquid are important to investigating reaction mechanisms. For in vitro studies of plasma-activated solutions, particularly those involving cell cultures, the liquid medium is typically in a small vessel, such as a single- or multiwell plate, that is exposed to a plasma source—a plasma jet or dielectric barrier discharge. A well plate is a plastic substrate with a matrix of small vials typically having diameters of 5–20 mm and depths of 5–20 mm. The liquid in these experiments can be as simple as distilled water to as complex as a cell culture medium. The chemical composition of the liquid is important not only for the formation of aqueous reactive species but also for the stability of the plasma-activated solution.

For example, Toyokuni et al.[22] investigated the components in cell culture medium RPMI-1640 that are responsible for the antitumor effect of PAM on ovarian cancer cells. They found that five out of the 38 medium components (Na_2HPO_4, $NaHCO_3$, L-tyrosine disodium salt dihydrate, L-histidine, and L-glutamine) produce the antitumor effect on the cancer cells, suggesting that these species may aid in the formation or stability of plasma produced reactive species in PAM. Tanaka et al.[23] also investigated the antitumor effects of plasma-activated-lactate (Ringer's solution) and showed that only the lactate in the solution contributes to its antitumor properties. Water activated by a plasma jet showed a correlation between the densities of aqueous reactive nitrogen species (RNS) and antibacterial effects.[14]

Generation and transport of RONS in the liquid occurs through several stages, which have their own dominating processes and timescales. The RONS in liquid can originate from the transport of gas-phase species from remote locations and their direct solvation into the liquid, or from the formation of species directly in the liquid or at the gas–liquid interface.[24,25] For instance, the generation of charged and excited species through electron impact ionization and excitation occurs in nanoseconds to microseconds. Some secondary reactive species such as O_3 and NO_x are generated during the plasma afterglow in microseconds to milliseconds.[26] The extended timescale may be long enough for these reactive species to reach the surface of a target (biological material) or a liquid medium and activate that surface despite the majority of primary species having already reacted away. Results from the modeling of argon plasma jets onto water by Verlackt et al.[27] showed that aqueous reactive species can either originate from the gas-phase plasma or be formed at the liquid interface. They found that densities of H_2O_{2aq}, $HNO_{2aq}/NO_2^-{}_{aq}$ and $NO_3^-{}_{aq}$ increase in solution as a function of time, while the densities of O_{3aq}, $HO_{2aq}/O_2^-{}_{aq}$, and $ONOOH_{aq}/ONOO^-{}_{aq}$ quickly saturate. (The subscript "aq" denotes an aqueous species.)

Long term evolution of the densities of gas-phase species can affect the final density of RONS in liquid. Dynamics and environmental factors that modify the plasma–liquid interaction may produce a change in PAM chemical properties (through transport of gas-phase species and their solvation) and eventually its biomedical effect. Studies have been performed on the influence of environmental parameters, such as the consequences of shielding gases on plasma jets[28–30] or the effect of touching and nontouching plasma jets with liquid.[31–33] Apart from the chemical composition of the gas and liquid, other environmental parameters including plasma jet geometry, liquid container topology, and its material properties can affect the dynamics of gas flow and the transport of species to the liquid layer. Gas flow can also induce mixing in the liquid and transport reactive species into deeper layers of the liquid. For example, experiments can be designed in which plasma jets interact with media

having a large surface to volume ratios (SVRs; e.g., Petri dishes or six-well plates) or small SVRs (e.g., microcentrifuge tubes or 96-well plates). Topological parameters such as width or depth of a plate affect the gas dynamics of the plasma jet, the propagation of ionization waves (IWs) to and on the liquid, and eventually the RONS production and distribution in the gas and liquid.

In this paper, we discuss results from a computational investigation of a helium atmospheric pressure plasma jet (APPJ) in contact with liquid water in a well plate. We assess the consequences of the height of a wall around a well (referred to as the well *rim*) on gas flow from the jet, the propagation of IWs, the subsequent plasma chemistry and its consequences on the solvated RONS in the water. After a description of the model and plasma jet setup (Section 2), the changes in flow, and production of RONS in the gas and liquid as a function of the height of the rim will be discussed following application of single-plasma pulses in Section 3. Results from multiple plasma pulses will be presented in Section 4. The outcomes of this study indicate that the water vapor density above the water layer increases with increasing rim height resulting in greater production of vapor dependent ROS such as OH and H_2O_2. High rims also induce vortices above the water layer that can increase transport of RONS to the water layer due to recirculation.

2 | DESCRIPTION OF THE MODEL

This computational investigation was performed with *nonPDPSIM*, a two-dimensional plasma hydrodynamics model using an unstructured, triangular mesh. As the model is described in detail by Norberg et al.,[33] it will be only briefly discussed here. Four modules in *nonPDPSIM* were employed for this investigation. Modified versions of the axisymmetric, compressible Navier–Stokes equations were used to model gas flow dynamics with implicit time steps on the order of μs. Poisson's equation (used to solve for electric potential) and continuity equations for charged species were integrated simultaneously to addresses plasma transport. The solution of Poisson's equation extends into all nonmetal materials. Charge is collected on the surfaces of the dielectrics (which have zero conductivity in the simulation) and included in the solution of Poisson's equation. The electron temperature was obtained by implicitly integrating an electron energy conservation equation accounting for collisions, convection and thermal conductivity. Stationary, two-term spherical-harmonic solutions of the Boltzmann equation were used produce electron impact rate coefficients and transport coefficients as a function of electron temperature. Finally, radiation transport was included to address

photoionization using a Greens function approach. The liquid layer in this simulation is computationally treated in a similar fashion to gas plasma, but with higher density and a different reaction mechanism. The liquid plasma region was assumed to be static, and fluid equations were not solved in the liquid. Transport of neutral species between gas and liquid zones is limited by Henry's law of equilibrium at the surface of the liquid. Gas-phase ions and photons are assumed to always cross the liquid/gas interface.[34] By definition, according to Henry's law, at equilibrium the density of a gas dissolved in a liquid is proportional to the density of that species in the gas phase, a ratio given by Henry's law constant, h: $n_l = n_g h$. When solvation of the gas-phase species saturates at the surface of the liquid, based on Henry's law of equilibrium, transport into the liquid ceases. When the liquid is supersaturated with a species at the surface, the aqueous species de-solvates into the gas phase. This equilibrium is calculated for the numerical nodes in the mesh on the surface of the liquid zone and their adjacent numerical nodes in the gas zone using an effective diffusion coefficient for transport.

After the discharge pulse terminates and the plasma decays to a small density, Poisson's equation is no longer solved and the simulation proceeds into the afterglow assuming the plasma is quasi-neutral. This investigation includes single- and multiple-discharge pulses. The first discharge pulse is fully simulated including the solution of Poisson's equation. However, for the second and subsequent pulses, the species resulting from the ns long discharge pulse are added as an instantaneous source at the start of each pulse. Poisson's equation is not solved, charge neutrality is enforced and the afterglow is computed for the interpulse period (determined by the pulse repetition frequency).[33]

The experimental APPJ that is the basis for simulation is a cylindrically symmetric jet reactor with two parallel ring electrodes that are covered with alumina dielectric. With this configuration, a discharge gap is formed in the middle of the gas flow tube as shown in Figure 1. This geometry approximates that of the *plasma pencil* developed by Laroussi and colleagues.[12,35,36] The feed gas is helium with dry air impurities flowing vertically downward through the tube into the humid ambient air. This configuration is adapted from the *plasma pencil* [35,36] with the following dimensions: 3-mm inner diameter of the tube, 5-mm discharge gap between the dielectric layers covering the electrodes, 1-cm length of the nozzle following the plasma cavity, and 1-cm distance between the nozzle and the water surface. The ring electrodes have radii of 5 mm and a thickness of 1 mm. The top electrode is powered by +30-kV pulses and the bottom electrode is grounded.

Photoionization is also included in this model due to its important role in the propagation of IWs with positive
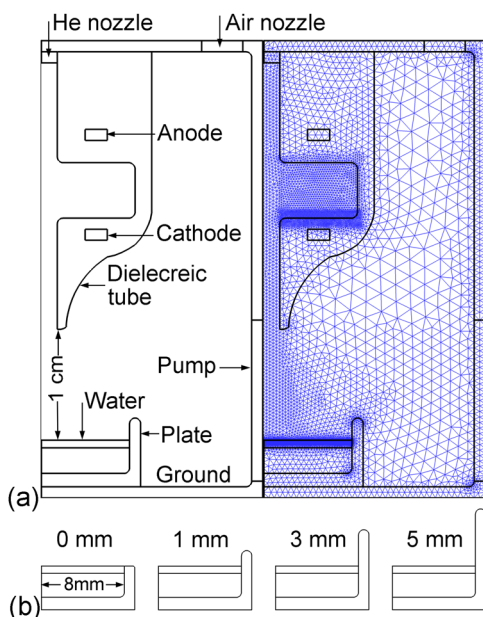
FIGURE 1 Cylindrically symmetric geometry of an atmospheric pressure plasma jet treating a single-well plate used in the model and computational mesh. (a) The top ring electrode is powered and the bottom electrode is grounded. The well plate has an 8-mm inner radius and the water layer has a thickness of 3 mm at a distance of 1 cm from the nozzle. Only the top 700 μm of the water is resolved as plasma. (b) The heights of the well plate rim are 0, 1, 3, and 5 mm

pulse polarity.[37,38] Photoionization of O_2 by the VUV flux from $N_2(a^1\Pi_g \rightarrow X^1\Sigma_g^+$, the Lyman–Birge–Hopfield system) and the photoionization of O_2, N_2, and H_2O from He_2^* VUV were included.[39] Secondary electron emission from positive ions incident on bounding surfaces of the plasma was included with a secondary emission coefficient $\gamma = 0.25$. Photoelectron emission from surfaces and photoionization of the liquid were not included.

The downward-directed He jet can deform the surface of the liquid and induce circulation in the liquid.[40] We have chosen a more simplified model with a nondeforming surface. We expect that for the high-rimmed cases, there would be little effect on the gas flow patterns due to the curvature of the liquid as recirculation is dominated by the vertical walls. For the flat plate, the curved surface would likely provide some upward slope to the radial flow across the plate. At atmospheric pressure, there is essentially a *no-slip* boundary condition for the velocity of the gas on the liquid surface relative to the speed of the surface. Although the liquid surface may actually be moving, the speed of the surface is very small compared to the gas above the boundary layer. A turbulence model has not been used for the bulk gas flow and so there may be enhanced mixing of the jet compared to that discussed here. However, for the Reynolds numbers for the flow in

this investigation, <800, we do not expect turbulence to be a major effect.

The entire computational domain (with computational mesh) shown in Figure 1a is 2×4.1 cm and contains over 12,000 numerical mesh nodes. The mesh is finer near the bottom electrode, water layer, and in the path of IW. The outer radial wall includes a pump (exit for the gas flow) and is electrically grounded, as is the surface under the well plate and the top surface of the computational domain. The two nozzles, helium, and ambient air, on top of the domain, are dielectrics. The APPJ feed and ambient gases initially flow for 70–100 ms to establish a steady-state flow field before the discharge. The feed gas is He, 99.97%, with O_2 and N_2 impurities (63 and 237 ppm) with a flow rate of 4 slm. Ambient humid air ($N_2/O_2/H_2O = 79.5/20/0.5$) flows through the coaxial nozzle around the APPJ at 2 slm to approximate air entrainment and reduce the occurrence of stagnation points in the volume outside the jet and above the well. The value of 2 slm was based on past experience and results are insensitive to the precise value of the coaxial flow.

The liquid layer in the well plate is water with 8-ppm dissolved O_2 and having a depth of 3 mm. However, only the top layer with a thickness of 700 μm is modeled as *liquid plasma*. The bottom portion of the water layer is a nominally solid material with the dielectric constant of water ($\varepsilon/\varepsilon_0 = 80$) to decrease the number of mesh nodes in plasma zones and increase computational speed. Evaporation from the water layer is included in the model by maintaining a water-saturated vapor pressure in the gas phase directly above the liquid region. The corresponding water vapor density is then used as a boundary condition for diffusive transport of water vapor from the liquid into the gas.[24]

The well plate has an 8-mm inner radius and a thickness of 1 mm with a dielectric constant of $\varepsilon/\varepsilon_0 = 10$ chosen to resemble the components of a commercial 24-well plate. The height of the well plate rim was varied from 0 to 5 mm from the water level, as shown in Figure 1b, without changing the distance between the water surface and the jet nozzle. Simulations were performed for rim heights of 0, 1, 3 and 5 mm. A selection of those results is discussed in the next section. A positive pulse of +30 kV with 350 ns width was applied (10 ns rise and fall times) in two modes—single pulse during which the Poisson's equation was solved and multiple pulses at 10 kHz with a total duration of 10 ms (100 pulses) during which the Poisson's equation was not solved. Following the last pulse, additional afterglow was computed for a total of 0.1 s.

The air and helium reaction mechanism used in this investigation contains 48 gas-phase species, 29 liquid

phase species, 905 gas-phase reactions, and 108 liquid reactions. In large part, the gas-phase reaction mechanism developed by van Gaens et al.[41] for argon APPJs interacting with humid air was used for the gas-phase portion of the mechanism with the addition of the helium reaction mechanism used previously by Norberg.[42] The water reaction mechanism is based on that of Lietz et al[43] and Tian et al.[24]

3 | PLASMA JET INTERACTION WITH WATER IN A WELL PLATE—SINGLE-DISCHARGE PULSE

When executing the model, the gas flow is simulated before initiating a discharge to stabilize a steady-state laminar flow. The resulting profiles of He, N_2 and H_2O vapor are shown in Figure 2a for rim heights of 0, 1, and 5 mm. The corresponding gas speeds and flow streamlines are shown in Figure 2b). The height of the rim (or in another point of view, the level of liquid in well plate) significantly affects the flow patterns of the plume of the APPJ, and as a result, affects the gas composition over and in a well plate. A flat plate (rim height 0 mm) resembles conventional APPJ treatment of flat surfaces. There is a stagnation point on the axis of the plume composed dominantly of He, with crossflow across the surface of the liquid. Evaporating water is entrained in the crossflow and transported away from the well plate, generally reducing the humidity. With the plume being narrow and boundary layer being thin, there is diffusion of O_2 and N_2 into the helium gas channel (gas flow out of the nozzle) and into the He boundary layer over the solution, which enables the production of RONS.

When increasing the rim height, the flow becomes progressively more stagnant in the well with a higher density of He and lower density of air, while inducing vortices that capture air and recirculate air into the vicinity of the well. For moderate rim heights, the recirculation of ambient air into the well is significant. The higher the rim of the well, the more confined the recirculation is to the well itself. This confined recirculation significantly reduces the transport of O_2 and N_2 to the liquid surface while trapping evaporating water vapor above the surface. The volume-averaged density of water vapor in the well increases with increasing the rim height. The flow is directed upwards by the plate rim, producing a vortex that recirculates helium (thereby filling the well) as well as creating a stagnation point at the intersection of the water layer and inside surface of the well. This vortex also entrains the ambient humid air into the well, which somewhat offsets the exclusionary
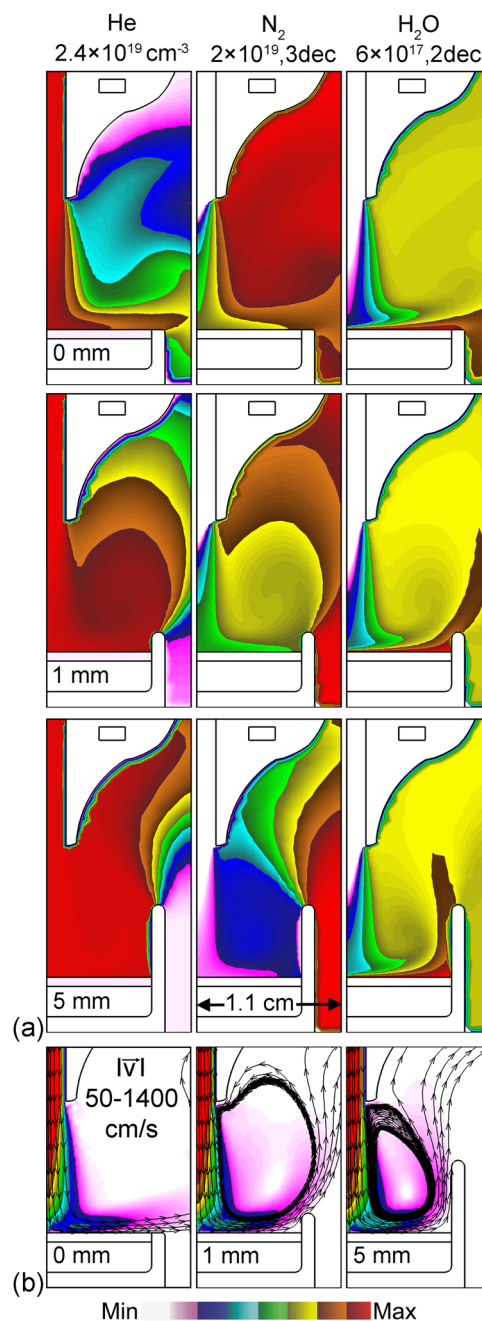
FIGURE 2 Flow properties before pulsing the discharge for well plates having 0, 1, and 5 mm rim heights. (a) He, N_2, and H_2O densities. (b) The speed and velocity streamlines (shown as contours). The maximum values are shown at the top with the number of decades noted if a log-scale

effect of the He stagnation flow. In going from a flat liquid surface to a 5-mm rim height, the densities of O_2 and N_2 above the liquid decrease by more than two orders of magnitude, whereas the water vapor density increases by a factor of 2.

After the flow is stabilized, a +30-kV pulse was applied to the top electrode to initiate the breakdown of the gas and propagation of an IW through the tube into
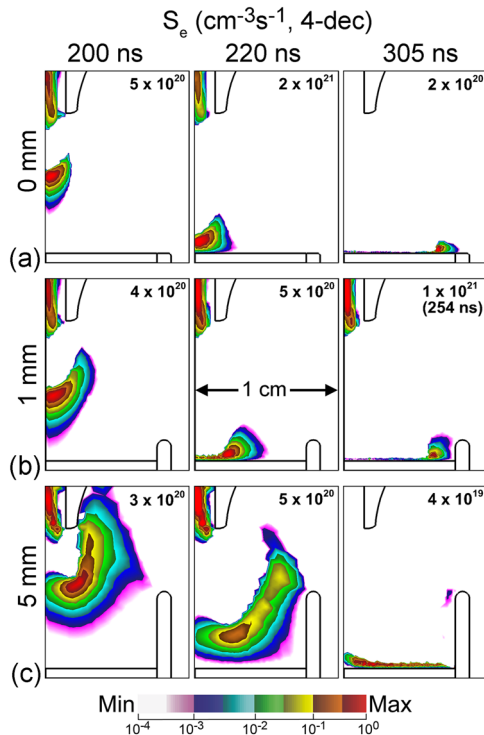
FIGURE 3 Electron impact ionization source (S_e) showing the progression of the volumetric ionization wave (IW) and surface ionization wave at times 200, 220, and 305 ns (unless noted) for well plates having rim heights of (a) 0 mm, (b), 1 mm, and (c) 5 mm. S_e is plotted on a log-scale over four decades with the maximum value shown in each frame. With a higher rim, the IW propagates more volumetrically

the ambient and incident onto the water. A cloud of plasma having a density of $10^{10}\,cm^{-3}$ and a radius of $100\,\mu m$ was seeded in the discharge gap in the vicinity of the powered electrode to initiate the discharge. Previous work showed that the magnitude of the plasma density in this cloud has little effect on the breakdown dynamics other than a time offset.[24] The plasma initiates in the gap between the two electrodes (discharge gap) within 20 ns. The head of the positive streamer propagates towards the cathode (grounded electrode) and charges the overlying dielectric. Surface ionization waves (SIWs) propagate on both the top and bottom dielectrics due to this surface charging. As the SIWs reach the edge of the on-axis tube, an IW is launched both upwards (against the gas flow) and downwards (with the gas flow). The downward IW propagates through the tube to emerge out of the nozzle, as shown in Figure 3. The IW propagating opposite the direction of helium flow has been experimentally observed by ICCD imaging.[44,45] The speed of the IW inside the jet is up to $10^7\,cm/s$, nearly independent of the plate geometry, a speed in the range of previous simulations and experimental measurements.[9,33,46] The speed of the IW is higher outside the

tube ($\sim2\times10^7\,cm/s$) due to the proximity of the ambient air, which enables additional ionization (i.e., Penning and photoionization), an observation which also agrees with experiments.

The propagation of the IW outside of the tube is sensitive to plate geometry (rim height). For example, the electron impact ionization sources, S_e, for plates having flat (0 mm), 1- and 5-mm rims are shown in Figure 3. With the flat plate, the He flows outside the tube as a well-defined jet surrounded by air as in conventional APPJs. The IW is largely confined to the helium gas channel due to the higher value of E/N (electric field/gas number density) required for the IW to spread laterally into the ambient air. This higher required E/N is due to the low lying vibrational and electronic states of molecular oxygen and nitrogen which result in electrons having a larger proportion of nonionizing energy loss collisions. Due to its low conductivity, the liquid behaves like a dielectric on nanosecond timescales—smaller than its dielectric relaxation time. After contacting the liquid layer, the plasma charges the water surface, producing horizontal components of the electric field. An SIW then propagates radially outwards on the surface of the water. This process is basically the same for the 1-mm rim height. However, with the 1-mm rim, the He gas channel above the liquid is broader, which then produces a larger diameter IW propagating towards the water layer. For a 1-mm rim, the boundary layer above the water is still well-defined and composed dominantly of He and water vapor as opposed to air. These conditions enable a SIW to propagate along the surface as in the absence of the rim or low rims.

As the rim height further increases, the well increasingly becomes filled with He with a less definitive boundary layer, and progressively produces a He-dominated volume above the well. In doing so, the source of confinement of the IW in the He column dissipates. That is, confinement of the IW by the surrounding shroud of air is limited. There is then a transition in the mode of IW propagation from being confined (the plasma-bullet mode) to spreading throughout the volume of the well plate. With the flat plate or short rim which produces a confined IW, the IW strikes the liquid essentially on-axis and spreads as an SIW over the liquid. With higher rimmed plates (3 and 5 mm), the IW propagates throughout the volume of the well plate above the water, arriving somewhat uniformly onto the gas–water interface. Propagation of a SIW with the high rim occurs only weakly.

For all rim heights, as the SIW travels along the surface of the liquid towards the corner of the plate, the magnitude of S_e increases (this is less apparent for a rim height of 5 mm due to the IW initially being volumetric).
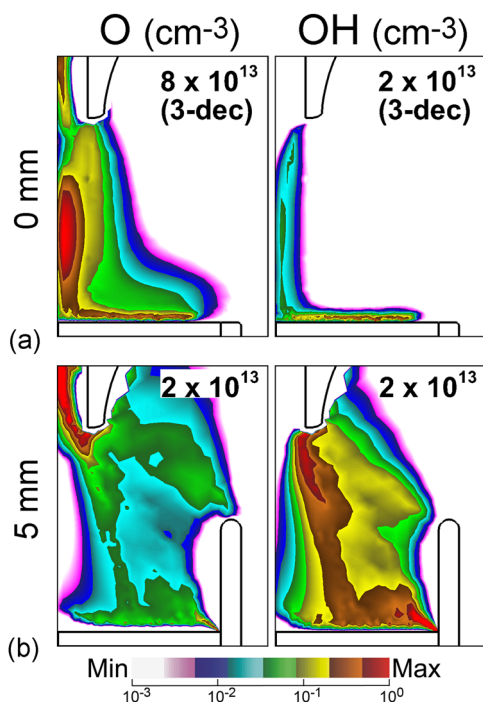
FIGURE 4 Densities of O and OH at 305 ns after the start of the discharge pulse for well plates having rim heights of (a) 0 mm and (b) 5 mm. The densities are plotted on a three-decade log-scale with maximum values noted in each figure

This increase in S_e is due to electric field enhancement at the edge of the well plate which resembles a triple point —the intersection of three materials which are conductive and significantly different dielectric constants. In these cases, the conductive material is the plasma itself, and the two dielectrics are the water and the wall (or rim) of the well. For all rim heights, there is also a higher water vapor density in the corner (or at the edge) of the well, which results in more net ionization than dry air.

The densities of O and OH are shown in Figure 4 at 305 ns, the time that the IW reaches its full extent, for rim heights of 0 and 5 mm. Oxygen atoms are initially formed inside the tube between the electrodes by electron impact dissociation of O_2 from the impurities in the feed gas. These O atoms are then transported out of the nozzle by the gas flow. The O atoms then react with the ambient air to form other RONS, including three-body reactions to generate O_3. The density of O inside the jet is the same order of magnitude for all plate geometries as the initial IW before leaving the nozzle is nearly independent of the rim height. Although there is a restrike IW that does depend on the geometry of the well plate, the restrike is not a major perturbation. The IW propagating outside the tube also produces O atoms. However that production depends on the mutual distributions of the IW and of the ambient O_2. With the flat plate, the IW is largely restricted to the He plume and along the surface of the

water. Electron impact dissociation of the O_2 diffusing into both the He plume and the He-dominated boundary layer then produces O atoms. The dissociation of water vapor produces few O atoms. However, the O density outside the jet decreases significantly with the increase of rim height due to the lower proximity of ambient O_2, as shown in Figure 4. The ambient O_2 diffuses into the He channel which enables O production by the IW by electron impact dissociation. With higher rims, He fills the well and displaces O_2, resulting in the density of O atoms above the water layer decreasing from 1×10^{14} (0-mm rim) to 3×10^{12} cm^{-3} (5-mm rim). This decrease in initial O atom density results in a lower O_3 density with increasing rim height.

In contrast to the trends with O (and O_3), the density of OH above the water increases with rim height. The initial production of OH is dominated by electron impact dissociation by the IW of H_2O diffusing into the He plume from the ambient and evaporating from the water layer. With low rims, the density of OH is localized either in the He column (H_2O density is low but intensity of the IW is high) or in the immediate proximity of water surface (~2×10^{12} cm^{-3}) where the water vapor density is high. With increasing rim height, the recirculation of He within the well entrains evaporating water vapor, producing a higher humidity above the water over a larger volume. Due to this effect, combined with a more diffuse IW, the density of OH on the surface and in the gas channel increases with increasing rim height. For example, with the 5-mm rim height, the distribution of OH follows that of the electron density, nearly filling the well plate to a density of 8×10^{12} cm^{-3}. One of the major pathways of H_2O_2 formation is through a three-body mediated mutual reaction of OH. As a result, the spatial profiles of H_2O_2 and OH are similar, resulting in the H_2O_2 density after the discharge pulse increasing with the height of the plate rim.

The RONS produced by the IWs immediately following the first discharge pulse undergo reactions in the gas flow field. The different gas dynamics of low- and high-rim plates result in significantly different outcomes during the afterglow. For example, the densities of RONS (OH, H_2O_2, O_3, and NO) are shown in Figure 5 at 10 ms into the afterglow following a single-discharge pulse for rim heights of 0, 1, and 5 mm. The gas flow for the flat plate has little recirculation, and generally flows radially outwards, which advects reactive species away from the plate. After 10 ms of flow, the maximum density of RONS produced by the single-discharge pulse is located off the plate due to this advection. Note that O_3 and NO, whose production requires O and N atoms, or excited states of N and N_2, still have substantial densities on-axis. These densities have not advected away. These densities result
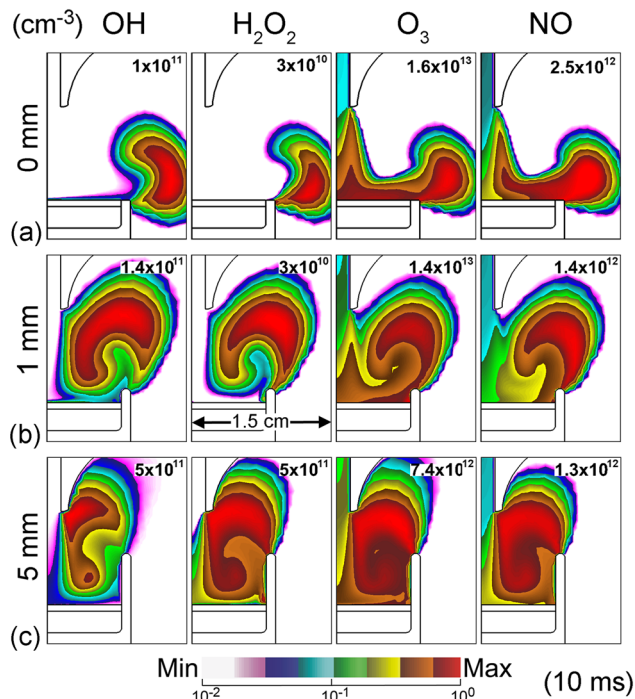
FIGURE 5 Densities of OH, H_2O_2, O_3, and NO at 10 ms after a single discharge pulse for well plates having rim heights of (a) 0 mm, (b) 1 mm, and (c) 5 mm. The densities are plotted on a two-decade log-scale with maximum values noted in each figure. Vortices are formed with the higher rims which recirculate the reactive oxygen and nitrogen species and fill the well plate with He

from O and N atoms (or excited states of N and N_2) produced in the tube and in the electrode cavity due to the small density of O_2 and N_2 impurities in the He flow. The O_3 and NO produced by these precursors then flow out of the electrode cavity and tube during the early afterglow.

In contrast, RONS densities during the afterglow with higher rim plates follow the vortex and so recirculate above the plate. These vortexed flows mix and fill the well plate and volume above the plate. With the additional residence time afforded by the recirculation, OH radicals have greater opportunity to react before flowing out of the domain, producing a significantly higher density of H_2O_2 at the boundary of the gas and liquid compared with the low-rim plate with which reactants advect away from the plate. This effect results in higher rates of solvation of RONS into the water with the high rim, to be discussed below. The production of H_2O_2 begins immediately after the discharge pulse and continues until OH is depleted. O_3 production continues during the afterglow due to O atoms continuing to flow out of the tube.

The production of higher order RNS is at a lower rate than ROS, and occurs dominantly during the afterglow

due to the larger number of reactions required for their formation. The maximum density of NO is higher and closer to the water–gas interface with the flat plate. The reason is that the densities of ROS species which react with N and O_2 to generate NO are higher near the water with the flat plate due to the SIW and penetration of ambient air into the boundary layer. Higher order RNS, such as NO_2 (nitrogen dioxide), have higher densities with the 5-mm rim plate. The density of NO_2 is higher by approximately a factor of 5 at 10 ms with the 5-mm rim compared to the flat rim for the same reason as production of H_2O_2. Recirculation extends the residence time of RNS in the vicinity of the water, and so the densities of species such as NO_2 that require several sequential reactions to produce are higher. These distinct changes in the dynamics of gas-phase reactive species as a function of geometry will affect the evolution of their counterpart aqueous species.
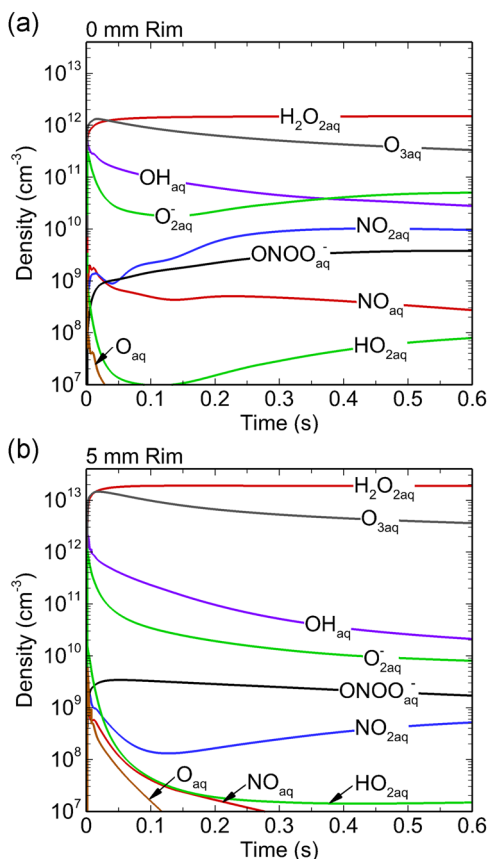
Following a single-discharge pulse, the gas dynamics convect RONS in the gas phase away from the plate in times of 10 to 100 ms, even with the high rim. Following the advection of the gas-phase RONS away from the surface, the evolution of solvated RONS occurs over a longer period. The volume-averaged densities in the liquid during 600 ms of afterglow following a single-discharge pulse are shown in Figure 6 for the flat (0 mm) and the high-rim (5 mm) plates. The "aq" subscript denotes an aqueous species and the rate coefficients (k) shown below are for 300 K with units of cm^3/s (1 cm^3/s is equivalent to $6.02 \times 10^{20}\,M^{-1} \cdot s^{-1}$) unless noted otherwise.

OH from the gas solvates into the water in milliseconds due to its large Henry's law constant, 6.92×10^2. The total density of OH in the gas phase above the water is an order of magnitude higher with the high rim due to the higher water vapor density in the well resulting from recirculation. These higher densities enable both more rapid solvation of OH to produce OH_{aq} and more production of gas-phase H_2O_2, both of which produce a larger inventory of H_2O_{2aq}. The density of H_2O_{2aq} is significantly higher with the high-rim plate. H_2O_{2aq} is produced either by the solvation of gas-phase H_2O_2 or by reactions:

$$OH_{aq} + OH_{aq} \rightarrow H_2O_{2aq} \quad (k = 1.7 \times 10^{-11}\,cm^3/s), \quad (1a)$$

$$H_{aq} + HO_{2aq} \rightarrow H_2O_{2aq} \quad (k = 3 \times 10^{-11} cm^3/s). \quad (1b)$$
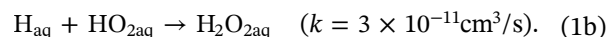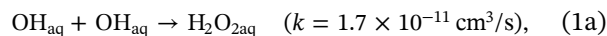
The H_2O_{2aq} density is $2 \times 10^{13}\,cm^{-3}$ after 600 ms with the high rim, an order of magnitude higher than for the flat plate, and correlates with its higher density in the gas phase. Having a large Henry's law constant (1.92×10^6), H_2O_2 has a large solvation capacity. For all practical purposes, H_2O_{2aq} will continue to increase in density as

FIGURE 6 Volume-averaged aqueous densities of reactive oxygen and nitrogen species during afterglow following a single-discharge pulse for well plates having rim heights of (a) 0 mm and (b) 5 mm

long as there is H_2O_2 available in the gas phase. However, in both geometries, the density of H_2O_{2aq} saturates in tens of milliseconds as the gas-phase H_2O_2 is depleted by convection and solvation, whereas the majority of OH_{aq} has already reacted to form H_2O_{2aq} and other RONS.

O_{3aq} is a relatively stable species and, after H_2O_{2aq}, has the highest density among ROS in water after 600 ms. Solvation of O_3 from the gas phase is the dominant source of O_{3aq}, followed by the solvation of atomic O and subsequent reaction with dissolved O_{2aq}. Due to its small Henry's law constant of 0.3, O_{3aq} saturates quickly within 10 ms into the afterglow, due to a combination of coming into equilibrium with the gas-phase O_3 density and O_3 being advected away from the water. Despite the initially lower production of O_3 in the gas phase with the high rim, the density of O_{3aq} reaches $4 \times 10^{12} \, \text{cm}^{-3}$ after 600 ms afterglow with the high rim, an order of magnitude higher than that with the flat plate. With the flat plate, gas-phase O_3 is advected away from the water, resulting in the liquid being supersaturated and then O_{3aq} desolvating into the gas phase. The increment in O_{3aq} density with the high rim can be through the
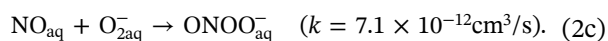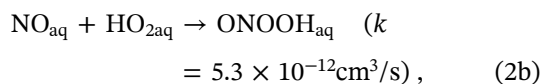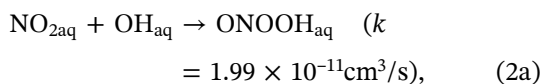
formation via $O_{aq} + O_{2aq} \rightarrow O_{3aq}$ ($k = 5 \times 10^{-12} \, \text{cm}^3/\text{s}$) in addition to gas recirculation which replenishes the near-water density of O_3. For these conditions, O atoms have a longer lifetime near the water with the high rim due to the lower density of O_2 in the well, which delays the conversion to O_3. The increase in O_{aq} with the high rim is an order of magnitude higher over several ms. The higher O_{aq}, in turn, contributes to the formation of O_{3aq} in water with the high-rim plate.

Note that in our reaction mechanism, solvated electrons (produced by the SIW on top of the water) quickly undergo charge transfer with solvated oxygen to form the superoxide anion ($O_2^-_{aq}$), which suppresses the density of solvated electrons. The lifetime of $O_2^-_{aq}$ is short in our system, tens of milliseconds,[47] which reduces its role as an oxidant and reductant in biological systems. The density of $O_2^-_{aq}$ is initially higher (by a factor of 3) with the high rim due to the higher electron density in the proximity of the water surface (the main source of $O_2^-_{aq}$ is solvated electron attachment to O_{2aq}). Having a high oxidation-reduction potential (reduction potential of 0.9 V), $O_2^-_{aq}$ is the precursor of many reactions including charge exchange to form OH^-_{aq} ($k = 1.5 \times 10^{-11} \, \text{cm}^3/\text{s}$) and $O_3^-_{aq}$ ($k = 2.6 \times 10^{-12} \, \text{cm}^3/\text{s}$); and oxidation reaction with NO_{aq} to form $NO_3^-_{aq}$ ($k = 6 \times 10^{-12} \, \text{cm}^3/\text{s}$) or $ONOO^-_{aq}$ ($k = 7 \times 10^{-12} \, \text{cm}^3/\text{s}$).[48] The other source of $O_2^-_{aq}$ is the hydrolysis of HO_{2aq} ($pKa = 4.8$) through $HO_{2aq} + H_2O_{aq} \rightarrow H_3O^+_{aq} + O_2^-_{aq}$ ($k = 1.4 \times 10^{-17} \, \text{cm}^3/\text{s}$). HO_{2aq} is produced by solvation from the gas phase, or through the reaction between H_{aq} and O_{2aq}, a slow process that proceeds in a few ms depending on the density of H_{aq} in the water. The majority of H_{aq} is produced by the solvation of H resulting from gas-phase electron impact dissociation of H_2O. These reactions occur at the highest rates when the SIW hugs the surface, as with the low-rimmed plates. Initially, the density of HO_{2aq} is smaller in the flat plate due to its lower density in gas phase. However, its density increases after 150 ms due to these longer timescale reactions, which then contribute to the formation $O_2^-_{aq}$, increasing its density.

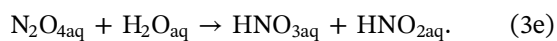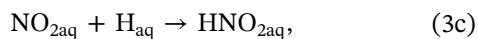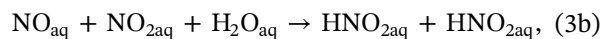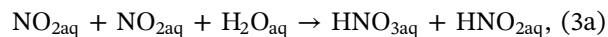RNS can be formed in both the gas and liquid phase. The dominant RNS are N_xO_y (NO, NO_2, NO_3, N_2O_3, N_2O_4, and N_2O_5) and acids (HNO_x), which evolve slowly during the afterglow with a time scale of a few milliseconds. The densities of solvated RNS such as $NO_{x \, aq}$ are higher with the flat plate. NO in the gas phase has a higher density close to the water surface for the flat plate due to the proximity of ambient air to the SIW. The higher flux of NO onto the water surface leads to an accumulation of NO_{aq}, which is then the precursor for higher-order RNS. For example, the reaction of NO_{aq} with OH_{aq} can produce $ONOO^-_{aq}$ (peroxynitrite) and

NO_{2aq}. NO_{aq} decays more slowly with the flat plate while its density drops by three orders of magnitude with the high rim. With the density of NO_2 being higher above the water with vortex-induced recirculation with the high rim, the larger flux of NO_2 onto water produces more NO_{2aq} after 100 ms. Nevertheless, the NO_{2aq} density at 600 ms with the high rim reaches only $5 \times 10^8 \, cm^{-3}$ which is significantly lower than $1 \times 10^{10} \, cm^{-3}$ with the flat plate.

$ONOO^-_{aq}$ is the conjugate base of peroxynitrous acid, $ONOOH_{aq}$ ($pKa = 6.8$), with a pH-dependent lifetime. (After a single-discharge pulse, there is no significant acidification of the liquid.) In our results, $ONOO^-_{aq}$ is among the highest density of solvated RNS. (Peroxynitrite is a toxic RONS which can cause protein oxidation, lipid peroxidation, and DNA and mitochondrial damage,[15] and is an antibacterial agent.[13]) With the flat plate, the density of $ONOO^-_{aq}$ increases to around $4 \times 10^9 \, cm^{-3}$ at 600 ms, whereas with the high rim its density is maximum after a few tens of ms after which it gradually decreases. The higher density of solvated NO_{2aq} and NO_{aq} with the flat plate yields more production of $ONOOH_{aq}$/ $ONOO^-_{aq}$.

$$NO_{2aq} + OH_{aq} \rightarrow ONOOH_{aq} \quad (k = 1.99 \times 10^{-11} cm^3/s), \quad (2a)$$

$$NO_{aq} + HO_{2aq} \rightarrow ONOOH_{aq} \quad (k = 5.3 \times 10^{-12} cm^3/s), \quad (2b)$$

$$NO_{aq} + O^-_{2aq} \rightarrow ONOO^-_{aq} \quad (k = 7.1 \times 10^{-12} cm^3/s). \quad (2c)$$

The high N_xO_y density with the flat plate leads to an order of magnitude larger HNO_{xaq} density through the following acid formation reactions[43]:

$$NO_{2aq} + NO_{2aq} + H_2O_{aq} \rightarrow HNO_{3aq} + HNO_{2aq}, \quad (3a)$$

$$NO_{aq} + NO_{2aq} + H_2O_{aq} \rightarrow HNO_{2aq} + HNO_{2aq}, \quad (3b)$$

$$NO_{2aq} + H_{aq} \rightarrow HNO_{2aq}, \quad (3c)$$

$$NO_{2aq} + OH_{aq} \rightarrow HNO_{3aq}, \quad (3d)$$

$$N_2O_{4aq} + H_2O_{aq} \rightarrow HNO_{3aq} + HNO_{2aq}. \quad (3e)$$

As a result, the density of HNO_{2aq} with the flat rim is $1 \times 10^8 \, cm^{-3}$, two orders of magnitude larger than that in the high-rim plate. Having said that, these are small densities, as might be expected after only a single-discharge pulse.

4 | PLASMA JET INTERACTION WITH WATER IN A WELL PLATE – REPETITIVE PULSING

Practical APPJs operate with a high repetition rate and extended exposure of samples to produce the desired dose. To model multiple discharge pulse exposure of the water, the simulation was performed for 100 pulses at a frequency of 10 kHz (100-μs interpulse period) as described in Section 2. The densities of O, O_3, H_2O_2, and NO_2 are shown in Figure 7 for the 10th, 50th, and 100th pulse. The left side of each figure shows densities with a flat plate and the right side shows densities with the 5-mm rim. The accumulation and consumption of gas-phase ROS and RNS during the 100 pulses are shown by the volume-averaged densities in Figures 8 and 9 for the flat and 5-mm rims. Long-lived species such as O_3 and H_2O_2 accumulate during the interpulse period in the gas phase and gradually solvate into the liquid, whereas transient species such as O and OH do not significantly accumulate as they undergo reactions to form other RONS. Convection does not significantly transport these species beyond the edge of the well plate in 10 ms. The maximum density of O atoms is inside the tube and in the helium channel, as shown in Figure 7. The density of O increases over about 50 pulses with both geometries (Figures 7 and 8). The depletion of O in each pulse is due to the oxidation reactions in the gas phase, predominantly O_3 formation, and solvation into water. With the high rim, O survives longer closer to the water, which increases its density at the gas–liquid interface. This is due to the lower density of O_2 near the water that would otherwise react with O to form O_3. This larger density of O with the high rim enhances solvation of O_{aq} and subsequent formation of O_{3aq}.

In contrast, O_3, H_2O_2, and NO accumulate in the gas phase over the course of 100 pulses because they are less reactive (Figures 7,9). O_3 production increases with the increase of cumulative input energy and the number of pulses. The formation of O_3 is a slow process and requires a few to tens of μs. Its production depends on the O atoms produced with each pulse and O_2 from the ambient air or the jet impurities. With the flat plate, ozone production jumps after the 10th pulse due to the convection of O atoms downward through the jet to where there is a higher density of O_2 to react with (Figure 7a). The density of O_3 reaches $10^{13} \, cm^{-3}$ with the flat plate, an order of magnitude larger than that of the high rim. With the flat plate having lateral flow across the surface, O_3 increases its density as it flows beyond the edge of the well. In contrast, the maximum density of O_3 is in the volume above the water with the high rim. The pattern of O_3 in the high rim at the 50th and 100th pulses

FIGURE 7 Densities of reactive oxygen and nitrogen species following 10, 50, and 100 discharge pulses with a 10-kHz pulse repetition rate for (a) O, (b) O_3, (c) H_2O_2, and (d) NO. The images show well plates having a flat (0 mm) rim on the left and a high (5 mm) rim on the right. Densities are plotted on a three-decade log-scale with the maximum value noted in each figure
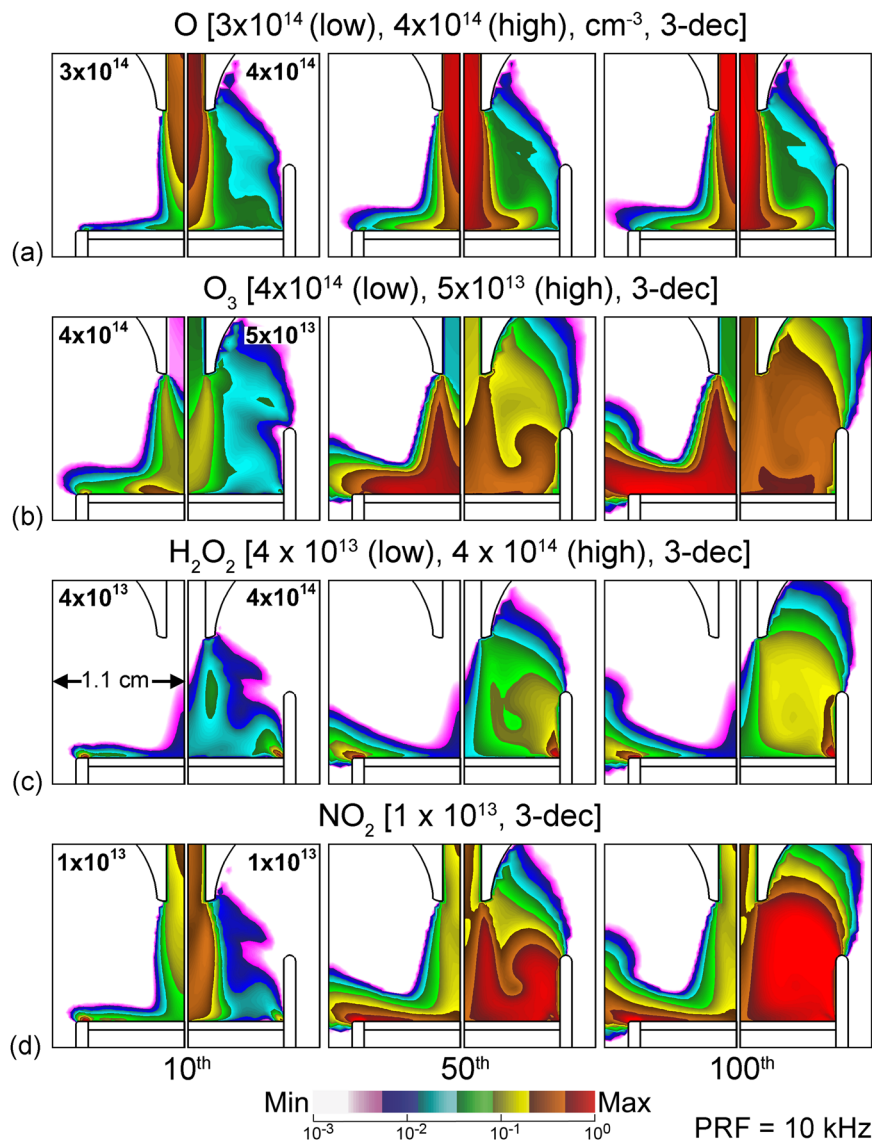
indicates that gas recirculation accumulates the residual ozone from previous pulses (Figure 7b).

The density of H_2O_2 follows the spatial distribution of OH and that of water vapor (Figure 7c). The density of OH reaches a quasi-steady state, with an impulsive increase and depletion with each pulse. At the end of 100 pulses, the density of OH is higher with the high rim by a factor of 7 (10^{12} cm^{-3}), whereas the density of H_2O_2 is larger by more than an order of magnitude. With the high rim, the density of H_2O_2 increases continuously, whereas with the flat plate the density of H_2O_2 quickly reaches a quasi-steady state (Figure 7c) and increasing by a factor of 5 compared with the first pulse. These differences are attributed to the accumulation of H_2O_2 above the water due to recirculation with the high rim, whereas gas-phase H_2O_2 is convected away from the water with the flat rim. Note that the densities H_2O_2 and NO_2 (discussed below) achieve a quasi-steady state above the water layer with

low rims due to their pulse periodic production and depletion by convection (Figure 7c,d). The volume-averaged densities of these species increase due to their accumulation beyond the well plate (Figures 8 and 9).
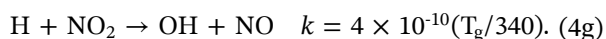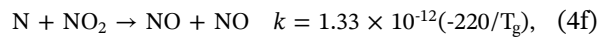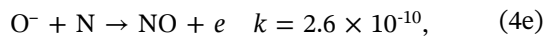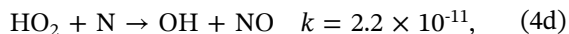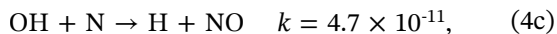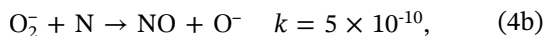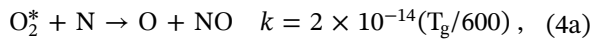
The average gas-phase densities of H_2 and HO_2 are higher in the high-rim plate by factors of 15 and 5 respectively as their formation depends on the dissociation of water vapor which is more plentiful above the water with the high rim (Figure 8). Although the densities of O, HO_2, and OH quickly saturate, the density of H_2, being less reactive, builds up over pulsing.

Repetitive pulsing is important for generating RNS due to the larger number of reactions required for their production. Nitric oxide primarily forms by reactions of excited states (O_2^* and N_2^*) with O_2 and N_2 during the discharge pulses, and during later pulses NO production dominated by NO_2 reactions through $N + NO_2 \rightarrow NO + NO$ and $O + NO_2 \rightarrow NO + O_2$. NO_2 is a transient species that is generated and consumed from pulse-to-pulse
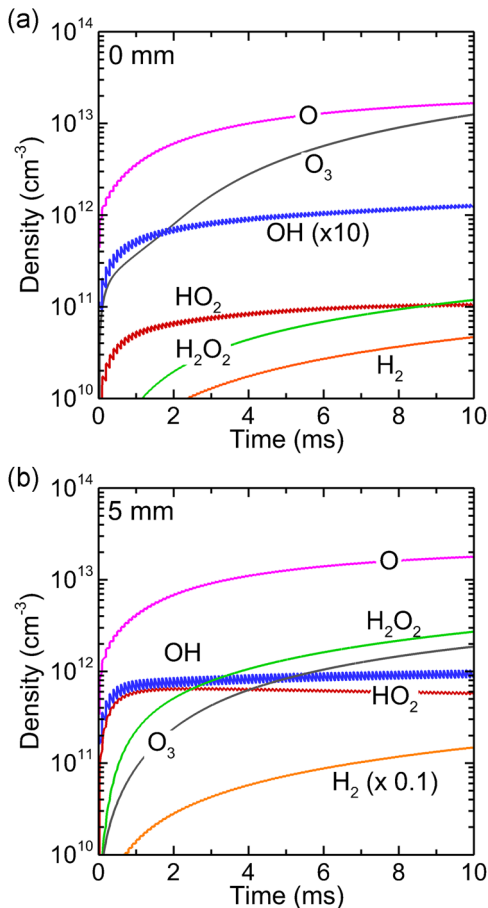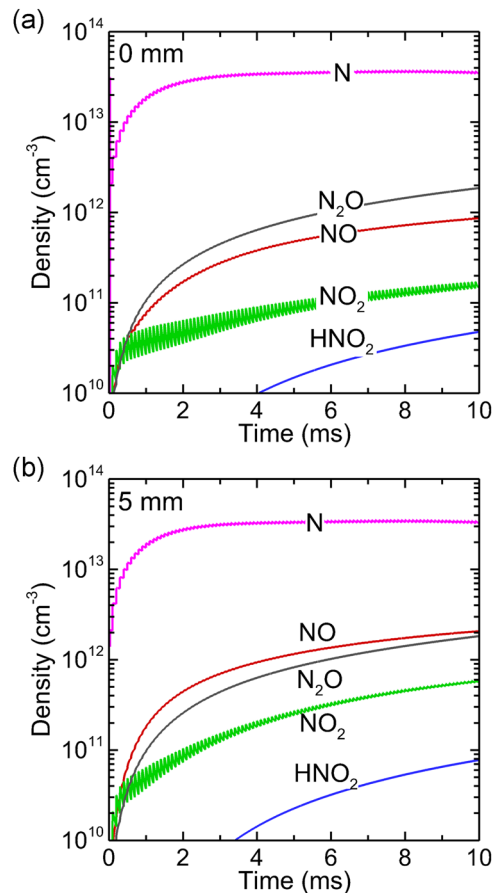
FIGURE 8 Densities of the reactive oxygen species in the gas phase during 100 pulses with a 10 kHz pulse repetition rate for well plates having rim heights of (a) 0 mm and (b) 5 mm. Densities are averaged over all gas volumes

FIGURE 9 Reactive nitrogen species densities in the gas phase during 100 pulses with a 10-kHz pulse repetition rate for well plates having rim heights of (a) 0 mm and (b) 5 mm. Densities are averaged over all gas volumes

while slowly accumulating densities (Figure 9). Other reactions that yield NO on a slower timescale include,

$$O_2^* + N \rightarrow O + NO \quad k = 2 \times 10^{-14}(T_g/600), \quad (4a)$$

$$O_2^- + N \rightarrow NO + O^- \quad k = 5 \times 10^{-10}, \quad (4b)$$

$$OH + N \rightarrow H + NO \quad k = 4.7 \times 10^{-11}, \quad (4c)$$

$$HO_2 + N \rightarrow OH + NO \quad k = 2.2 \times 10^{-11}, \quad (4d)$$

$$O^- + N \rightarrow NO + e \quad k = 2.6 \times 10^{-10}, \quad (4e)$$

$$N + NO_2 \rightarrow NO + NO \quad k = 1.33 \times 10^{-12}(-220/T_g), \quad (4f)$$

$$H + NO_2 \rightarrow OH + NO \quad k = 4 \times 10^{-10}(T_g/340). \quad (4g)$$

After 100 pulses, NO in the gas phase is larger with the high-rim plate by a factor of 2 compared to the flat plate. The maximum density of NO is located above the water layer with the flat plate, which only moderately accumulates with pulsing due to the advective flow across the water.

After the first pulse, NO_2 has the highest density among the RNS and is independent of plate geometries as its density depends on the plasma processes in the tube and there are few other long-lived species to react with. With multiple pulses, NO_2 is formed and consumed from pulse-to-pulse to generate other RNS and therefore does not accumulate significantly as shown in Figure 9. This trend is more pronounced with the flat plate where NO_2 reaches a quasi-steady state by 40 pulses after which the radial flow blows NO_2 to the exit. In the high rim, NO_2 recirculates above the water layer and fills the well plate (Figure 7). Therefore, the density of NO_2 is higher with the high rim by a factor of 3 (1×10^{12} cm^{-3}) after the 100th pulse. The accumulation of NO_2 with the high rim can enhance the formation of HNO_2 which then solvates having a markedly larger Henry's law constant (1.15×10^3) compared to NO_x.

Similar to O, the production and distribution of atomic nitrogen N are independent of plate geometries. Atomic nitrogen that is formed by electron impact dissociation is not very reactive at ambient temperatures and does not contribute significantly to N_xO_y formation. The density of N reaches a steady-state within 20 pulses with the same magnitude for flat and high-rim geometries (Figure 9). A large fraction of N simply recombines to N_2 or to a lesser degree reacts with ROS to form NO, N_2O, and HNO_x. The magnitude of N_2O (nitrous oxide) in the gas phase is similar in both geometries, as it accumulates over pulsing by being less reactive than NO_2. Its density is higher where O is available, which is predominantly inside the tube and He gas channel. N_2O is gradually generated with the increase of N in the gas channel. The main two pathways to N_2O formation are $N + NO_2 \rightarrow N_2O + O$ ($k = 1.66 \times 10^{-12}(-220/T_g)$) and $O^- + N_2 \rightarrow N_2O + e$ ($k = 1 \times 10^{-12}$). Other RNS (NO_3, N_2O_3, N_2O_4, and N_2O_5) and acids HNO_x form slowly during the afterglow, and so are enhanced by the high-rim plate due to higher NO_x resulting from recirculation. For example, the densities of N_2O_3 and N_2O_4 are approximately an order of magnitude larger with the high rim.

Densities of selected aqueous species are shown in Figure 10 after 100 pulses. During the 100 pulses of treatment, there is some acidification of the liquid. For the flat plate, the pH decreases to 6.3. For the high-rim plate, the pH decreases to 5.8. O_{3aq} in water saturates quickly due to its relatively low Henry's law constant ($h = 0.3$). It is expected that the higher O_3 densities adjacent to the water layer and initial higher rate of solvation of O with the flat plate would produce a higher solvated ozone density. This is the case for short times (up to the 14th pulse) as shown in Figure 10a. However, the density of O_{3aq} is moderately higher with the high rim after 100 pulses (3×10^{13} cm^{-3}) due to the recirculation of O_3 back to the water layer. Although O_{3aq} is more stable in acidic solutions the small decrease in pH is not significant in quenching O_{3aq} for these timescales.[49] The volume-averaged density of H_2O_{2aq} is a factor of 5 larger with the high rim due the higher density of H_2O_2 in the gas phase resulting from recirculation.
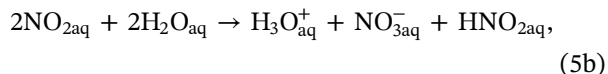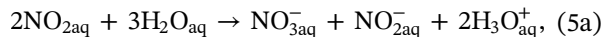
At the end of the 100th pulse, the densities of RNS (including $NO_3^-{}_{aq}$, N_2O_{5aq}, HNO_{2aq}, and $ONOOH_{aq}$) are higher with high-rim plates compared to the flat plate. These increases in densities are by a factor of 2–5. For these conditions, the intermediate 3-mm high-rim yields higher aqueous densities of RNS than the 5-mm rim. With the 3-mm rim, there is sufficient recirculation from the ambient bringing N_2 near the water layer where densities of O and OH are also large to produce HNO_x gas-phase precursors. With the 5-mm rim, the volume above the water layer is dominated by the incident gas plume of recirculating He, which excludes N_2 from the
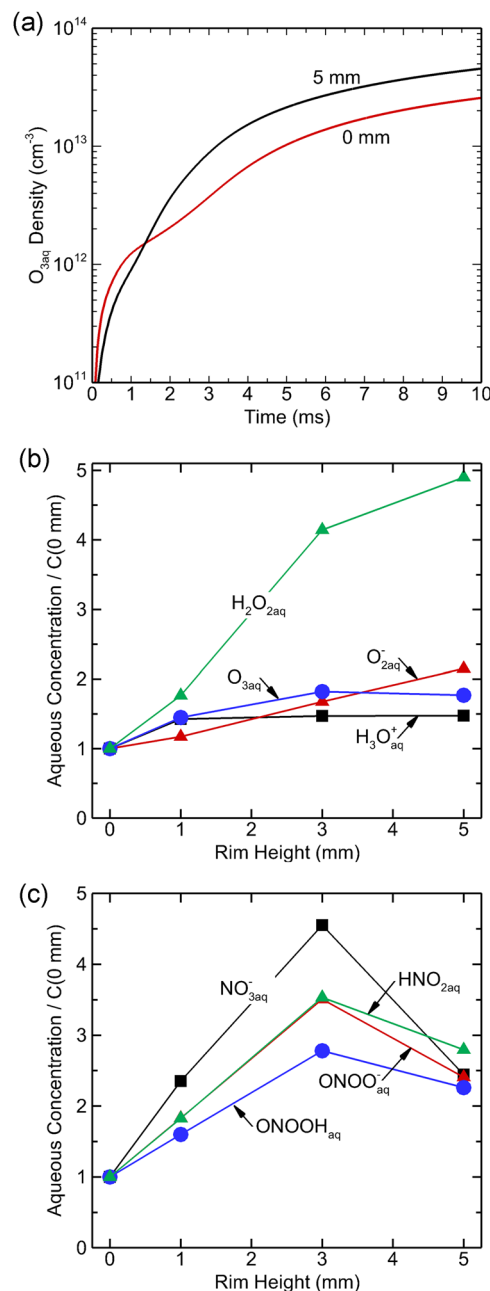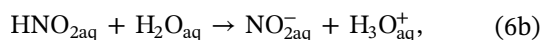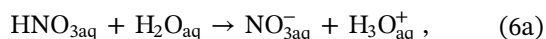

FIGURE 10 Density of solvated species for well plates with different rim heights during and after 100 pulses with a 10 kHz pulse repetition rate. (a) O_{3aq} for well plates with flat (0 mm) and high (5 mm) rims as a function time during 100 pulses (10 ms). The densities of solvated reactive oxygen and nitrogen species at the end of the 100th pulse for well plates having 0-, 1-, 3- and 5-mm rim heights shown for those species with densities that (a) increase with rim height and (b) have a maximum at an intermediate rim height. The values are normalized to that for the flat plate (0 mm)

well, and is a barrier to recirculation of products coming back into the well. NO_{aq} is higher by a factor of 2–5 for the 3-mm rim, whereas the density of $NO_2^-{}_{aq}$ density is about the same for both plates. $NO_3^-{}_{aq}$ and $NO_2^-{}_{aq}$ are

formed in plasma-activated water through the solvation of NO_x from the gas phase and the hydrolysis of NO_x in water that produces $H_3O^+_{aq}$ ions in water (Equation 5).

$$2NO_{2aq} + 3H_2O_{aq} \rightarrow NO^-_{3aq} + NO^-_{2aq} + 2H_3O^+_{aq}, \quad (5a)$$

$$2NO_{2aq} + 2H_2O_{aq} \rightarrow H_3O^+_{aq} + NO^-_{3aq} + HNO_{2aq}, \quad (5b)$$

as well as acid dissociation,

$$HNO_{3aq} + H_2O_{aq} \rightarrow NO^-_{3aq} + H_3O^+_{aq}, \quad (6a)$$

$$HNO_{2aq} + H_2O_{aq} \rightarrow NO^-_{2aq} + H_3O^+_{aq}, \quad (6b)$$

$$ONOOH_{aq} + H_2O_{aq} \rightarrow ONOO^-_{aq} + H_3O^+_{aq}. \quad (6c)$$

The densities of some solvated RONS that are of interest in biomedical applications are shown in Figure 10b,c at the end of the 100 pulses for different rim heights. The density of H_2O_{2aq} increases by a factor of 5 for the high rim compared to the flat plate. It has been shown that there is correlation between cells and bacteria

death and H_2O_{2aq} concentration.[13,36] These findings suggest that a subtle change in the experimental configuration can induce a meaningful change in the final concentration of ROS in PAM and the final biological disposition. The densities of O_{3aq} and $O_2^-{}_{aq}$ also moderately increase with rim height from 0 to 5 mm. For both species, the increase in their density depends not only on the solvation from the gas phase but also on their formation in the water. The OH_{aq} density also increases with rim height by 30% but the effect is smaller than for H_2O_{2aq} because the lifetime of its precursor OH in the gas phase is much shorter than that of H_2O_{2aq}. The density of $ONOO^-{}_{aq}$ also increases with rim height with the exception of the 5-mm rim. This trend could be due to competing formation and destruction pathways with increasing rim height. For instance with the 5-mm rim height, the lower NO_{aq} density coupled with an insufficient density of OH_{aq} could result in a lower density of $ONOO^-{}_{aq}$.

The densities of gas-phase H_2O_2 and HNO_2 after 100 discharge pulses and 25 ms of afterglow are shown in Figure 11 for rim heights from 0 to 5 mm. Following the end of the discharge pulse, the production of H_2O_2 ends, as its short-lived precursor, OH, is no longer being
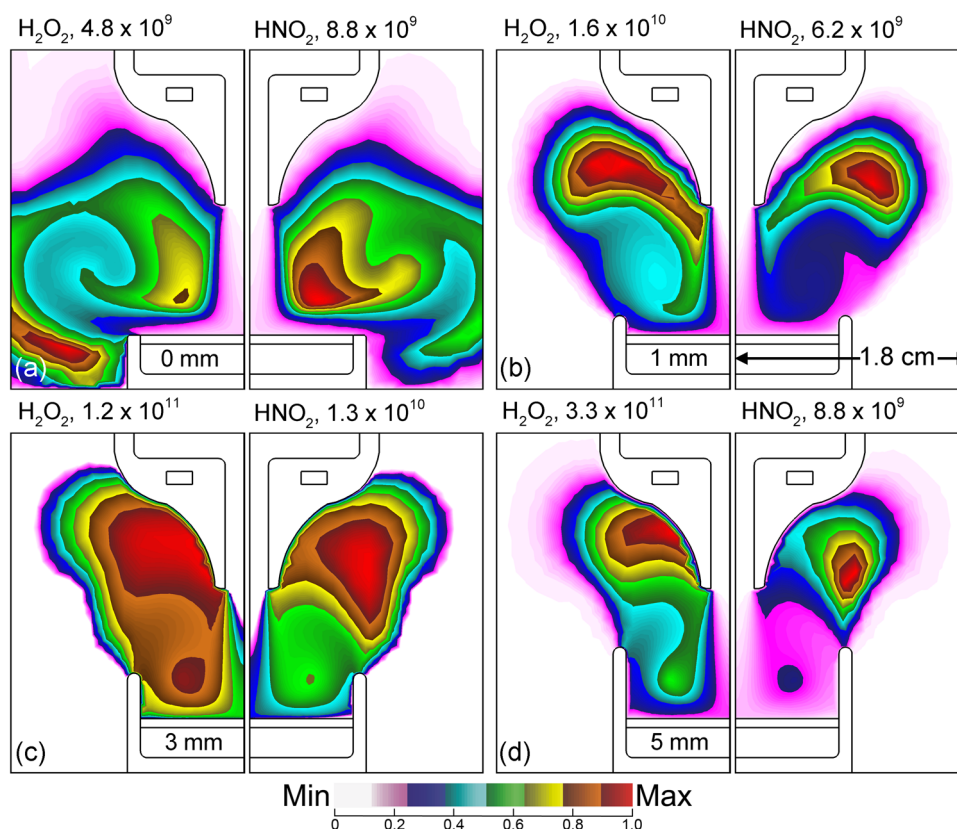
FIGURE 11 Densities of gas-phase species at 25 ms following 100 discharge pulses at a 10-kHz pulse repetition rate for well plates having rim heights of (a) 0 mm, (b) 1 mm, (c) 3 mm, and (d) 5 mm. The densities of H_2O_2 are shown on the left and for HNO_2 on the right. The maximum values are shown in each frame
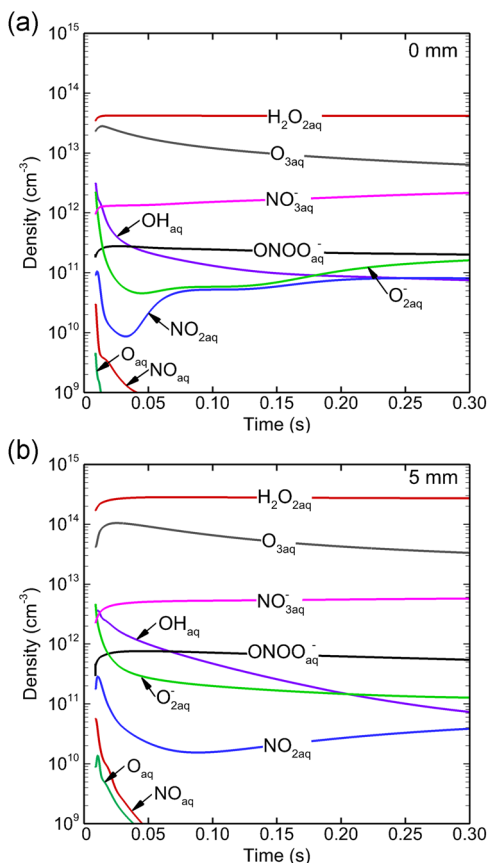
FIGURE 12   Aqueous densities of reactive oxygen and nitrogen species during the afterglow following 100 discharge pulses at 10 kHz for well plates having rim heights of (a) 0 mm and (b) 5 mm

generated. The generation of HNO_2 continues during the afterglow due to its longer-lived precursors. The recirculation and vortexing patterns of the gas then redistribute these species. With the advective flow across the surface of the flat and short-rimmed plates, there is little H_2O_2 and HNO_2 which circulates back to the water, and so there is little additional solvation into the liquid during the afterglow. The higher rimmed plates continue to recirculate H_2O_2 and HNO_2 to the water layer, enabling solvation of these species long into the afterglow.

The volume-averaged afterglow densities of aqueous RONS following 100 pulses and afterglow totaling 300 ms are shown in Figures 12a and 12b for the flat and 5-mm high-rim plates. The trend of aqueous phase species in Figure 12 over 300 ms is qualitatively similar to the afterglow from a single pulse shown in Figure 6. In the plasma-activated water, the change in densities of most species is due to reactions rather than transport. Desolvation into the gas can occur for over-saturated species, which is not a major effect in our system other than for O_3. The most abundant ROS for both rim heights is H_2O_{2aq}, and the most abundant RNS is $NO_3{}^-{}_{aq}$. For

these conditions, H_2O_{2aq} and $NO_3{}^-{}_{aq}$ are stable for the simulated time (300 ms afterglow). H_2O_{2aq} is larger by an order of magnitude, reaching a density of $3 \times 10^{14} \, cm^{-3}$ and $NO_3{}^-{}_{aq}$ is larger by a factor of 3 for the high-rim plate, reaching a density of $6 \times 10^{12} \, cm^{-3}$. O_{3aq}, the second most abundant ROS, has a higher density by a factor of 4 with the high-rim plate. This is in part due to the slower rate of desolvation of O_{3aq}. With O_3 quickly removed by advection from the surface of the flat plate, O_{3aq} appears to be more supersaturated (even for the same in-liquid density) and so it de-solvates at a higher rate.

The density of $NO_3{}^-{}_{aq}$ is buoyed during the afterglow due to the solvation of $(H)NO_x$ followed by hydrolysis (Equation 5). The recirculation of $(H)NO_x$ with the high-rim plates during the afterglow maintains its solvation. For example, the density of HNO_3 continues to recirculate during the afterglow. Due to the high Henry's law constant of this species ($h = 4.8 \times 10^6$), the liquid does not saturate, which then yields more $NO_3{}^-{}_{aq}$ by hydrolysis. The density of $ONOO{}^-{}_{aq}$ also increases with multiple-pulsing by a factor of 15 for both flat and high-rim plates although its density is relatively constant during the afterglow. O_{aq} is short-lived in water due to its rapid reaction with O_{2aq} to form O_{3aq}. Due to the low Henry's law constant for O_3, this reaction can be the major source of O_{3aq}. As a result of this rapid conversion of O_{aq} to O_{3aq}, the density of O_{aq} decays to negligible values within tens of ms. Consumption of O atoms in the gas phase before their solvating can actually decrease the rate of production of O_{3aq}. For example, flow conditions that provide a large flux of O atoms from the jet to the surface of the water but exclude reactants from the ambient will minimize consumption of O in the gas phase, leaving more to solvate to produce O_{3aq}. With a small Henry's law constant for O_3, it is then possible to supersaturate the surface of the liquid with O_{3aq}, which would result in the desolvation of O_{3aq} into the gas phase.

5 | CONCLUDING REMARKS

The properties of a helium plasma jet in contact with water in a dielectric well plate and the consequences of the plate rim height on RONS densities in the gas and liquid phases were discussed using results from a computational investigation. The outcome of this investigation emphasizes the importance of specifying geometric details of experimental set-ups (e.g., height of rim on the well plate or, equivalently, the depth of the liquid) on reproducibility of experiments and the ability to compare measurements and control production of RONS in the gas and liquid. The discharges in this investigation

used +30 kV, 350-ns pulse widths with single- and 100-pulse excitations, followed by afterglows of up to 600 ms.

Rim heights of 0–5 mm were examined. With low rims, the gas flow patterns generally retained a jet-like column of He, which advected across the surface of the liquid with a thin boundary layer. Evaporating water was largely restricted to the boundary layer. The bulk IW and following SIW were then generally confined to the axis and along the surface of the liquid. The ambient humid air was able to penetrate into the He column and surface boundary layer, however, little air was recirculated by vortices. With the highest rims, the well was filled with He and evaporating water. There was little advection across the water while vortices recirculated humid air and reaction products back to the well. Upon exiting the nozzle of the jet, the bulk IW broadened and arrived at the liquid fairly uniformly across the surface. The following SIW was nominal.

The solvation of plasma produced reactive species into the liquid are sensitive to these flow patterns, tempered by their Henry's law constants. For example, the density of O_3 above the water is higher with the flat plate due to the proximity of O and O_2 but the long term density of solvated O_{3aq} increases with the rim height due to recirculation which brings O_3 back to the surface. With there being a larger production of O_{aq} wtih the high rim, there is also greater in water production of O_{3aq}. Desolvation is important for this low Henry's law constant species. With the flat plate, advection reduces the density of O_3 above the liquid, which leaves the water supersaturated with O_{3aq} to a greater degree than with the high rim for which O_3 is recirculated back to the well. This recirculation and increased residence time near the water is particularly important for gas-phase species that require several reactions to produce and which have high Henry's law constants. These species are typically RNS. The density of select RNS in the water may be higher with the lower rim following a single-discharge pulse because of the higher penetration of N_2 into the helium channel and boundary layer. However, when repetitively pulsing over long times, recirculation produces larger aqueous densities of high Henry's law RNS. As a result, the density of HNO_{xaq} was larger for high-rim plates by an order of magnitude compared to flat rims.

ACKNOWLEDGMENTS

ORCID

Soheila Mohades http://orcid.org/0000-0002-4719-8275
Amanda M. Lietz http://orcid.org/0000-0001-6423-5042
Juliusz Kruszelnicki http://orcid.org/0000-0003-4596-1780
Mark J. Kushner http://orcid.org/0000-0001-7437-8573

REFERENCES

[1] E. A. Ratovitski, X. Cheng, D. Yan, J. H. Sherman, J. Canady, B. Trink, M. Keidar, *Plasma Process. Polym.* **2014**, *11*, 1128.

[2] M. Vandamme, E. Robert, S. Lerondel, V. Sarron, D. Ries, S. Dozias, J. Sobilo, D. Gosset, C. Kieda, B. Legrain, J. M. Pouvesle, A. L. Pape, *Int. J. Cancer* **2012**, *130*, 2185.

[3] F. Utsumi, H. Kajiyama, K. Nakamura, H. Tanaka, M. Mizuno, K. Ishikawa, H. Kondo, H. Kano, M. Hori, F. Kikkawa, *PLOS One* **2013**, *8*, e81576.

[4] M. Keidar, R. Walk, A. Shashurin, P. Srinivasan, A. Sandler, S. Dasgupta, R. Ravi, R. Guerrero-Preston, B. Trink, *Br. J. Cancer* **2011**, *105*, 1295.

[5] A. G. Lin, B. Xiang, D. J. Merlino, T. R. Baybutt, J. Sahu, A. Fridman, A. E. Snook, V. Miller, *Oncoimmunology* **2018**, *7*, e1484978.

[6] L. I. Partecke, K. Evert, J. Haugk, F. Doering, L. Normann, S. Diedrich, F. U. Weiss, M. Evert, N. O. Huebner, C. Guenther, C. D. Heidecke, A. Kramer, R. Bussiahn, K. D. Weltmann, O. Pati, C. Bender, W. von Bernstorff, *BMC Cancer* **2012**, *12*, 473.

[7] S. Takeda, S. Yamada, N. Hattori, K. Nakamura, H. Tanaka, H. Kajiyama, M. Kanda, D. Kobayashi, C. Tanaka, T. Fujii, M. Fujiwara, M. Mizuno, M. Hori, Y. Kodera, *Ann. Surg. Oncol.* **2017**, *24*, 1188.

[8] D. Yan, H. Cui, W. Zhu, N. Nourmohammadi, J. Milberg, L. G. Zhang, J. H. Sherman, M. Keidar, *Sci. Rep.* **2017**, *7*, 4479.

[9] M. Keidar, A. Shashurin, O. Volotskova, M. Ann stepp, P. Srinivasan, A. Sandler, B. Trink, *Phys. Plasmas* **2013**, *20*, 57101.

[10] S. U. Kang, J. H. Cho, J. W. Chang, Y. S. Shin, K. I. Kim, J. K. Park, S. S. Yang, J. S. Lee, E. Moon, K. Lee, C. H. Kim, *Cell Death Dis.* **2014**, *5*, e1056.

[11] F. Judée, C. Fongia, B. Ducommun, M. Yousfi, V. Lobjois, N. Merbahi, *Sci. Rep.* **2016**, *6*, 21421.

[12] S. Mohades, M. Laroussi, V. Maruthamuthu, *J. Phys. D: Appl. Phys.* **2017**, *50*, 185205.

[13] P. Lukes, E. Dolezalova, I. Sisrova, M. Clupek, *Plasma Sources Sci. Technol.* **2014**, *23*, 15019.

[14] P. Shaw, N. Kumar, H. S. Kwak, J. H. Park, H. S. Uhm, A. Bogaerts, E. H. Choi, P. Attri, *Sci. Rep.* **2018**, *8*, 11268.

[15] L. Adams, M. C. Franco, A. G. Estevez, *Exp. Biol. Med. (Maywood)* **2015**, *240*, 711.

[16] S. F. AbdulSalam, F. S. Thowfeik, E. J. Merino, *Biochemistry* **2016**, *55*, 5341.

[17] S. Heinzelmann, G. Bauer, *Biol. Chem.* **2010**, *391*, 675.

[18] D. B. Graves, *Phys. Plasmas* **2014**, *21*, 80901.

[19] C. F. Nathan, S. C. Silverstein, L. H. Brukner, Z. A. Cohn, *J. Exp. Med.* **1979**, *149*, 100.

[20] N. Kurake, H. Tanaka, K. Ishikawa, T. Kondo, M. Sekine, K. Nakamura, H. Kajiyama, F. Kikkawa, M. Mizuno, M. Hori, *Arch. Biochem. Biophys.* **2016**, *605*, 102.

[21] V. S. S. K. Kondeti, C. Q. Phan, K. Wende, H. Jablonowski, U. Gangal, J. L. Granick, R. C. Hunter, P. J. Bruggeman, *Free Radic. Biol. Med.* **2018**, *124*, 275.

[22] S. Toyokuni, F. Kikkawa *Plasma Medical Science* (Eds: S. Toyokuni, Y. Ikehara, F. Kikkawa, M. Hori), Academic Press, **2019**, pp. 249–318.

[23] H. Tanaka, K. Nakamura, M. Mizuno, K. Ishikawa, K. Takeda, H. Kajiyama, F. Utsumi, F. Kikkawa, M. Hori, *Sci. Rep.* **2016**, *6*, 36282.

[24] W. Tian, M. J. Kushner, *J. Phys. D: Appl. Phys.* **2014**, *47*, 165201.

[25] P. Bruggeman, C. Leys, *J. Phys. D: Appl. Phys.* **2009**, *42*, 53001.

[26] X. Lu, G. V. Naidis, M. Laroussi, S. Reuter, D. B. Graves, K. Ostrikov, *Phys. Rep.* **2016**, *630*, 1.

[27] C. C. W. Verlackt, W. van Boxem, A. Bogaerts, *Phys. Chem. Chem. Phys.* **2018**, *20*, 6845.

[28] A. Schmidt-Bleker, J. Winter, S. Iseni, M. Dünnbier, K.-D. Weltmann, S. Reuter, *J. Phys. D: Appl. Phys.* **2014**, *47*, 145201.

[29] H. Jablonowski, M. A. Ch. Hänsch, M. Dünnbier, K. Wende, M. U. Weltmann, S. Reuter, T. von Woedtke, *Biointerphases* **2015**, *10*, 29506.

[30] A. Schmidt-Bleker, S. A. Norberg, J. Winter, E. Johnsen, S. Reuter, K. D. Weltmann, M. J. Kushner, *Plasma Sources Sci. Technol.* **2015**, *24*, 35022.

[31] V. S. S. K. Kondeti, U. Gangal, S. Yatom, P. J. Bruggeman, *J. Vac. Sci. Technol. A* **2017**, *35*, 61302.

[32] S. A. Norberg, W. Tian, E. Johnsen, M. J. Kushner, *J. Phys. D: Appl. Phys.* **2014**, *47*, 475203.

[33] S. A. Norberg, E. Johnsen, M. J. Kushner, *Plasma Sources Sci. Technol.* **2015**, *24*, 35026.

[34] W. Tian, A. M. Lietz, M. J. Kushner, *Plasma Sources Sci. Technol.* **2016**, *25*, 55020.

[35] M. Laroussi, T. Akan, *Plasma Process. Polym.* **2007**, *4*, 777.

[36] S. Mohades, N. Barekzi, H. Razavi, V. Maruthamuthu, M. Laroussi, *Plasma Process. Polym.* **2016**, *13*, 1206.

[37] X. Lu, K. Ostrikov, *Appl. Phys. Rev.* **2018**, *5*, 31102.

[38] S. Nijdam, F. M. J. H. van de Wetering, R. Blanc, E. M. van Veldhuizen, U. Ebert, *J. Phys. D: Appl. Phys.* **2010**, *43*, 145204.

[39] A. Lofthus, P. H. Krupenie, *J. Phys. Chem. Ref. Data* **1977**, *6*, 113.

[40] P. Heirman, W. Van boxem, A. Bogaerts, *Phys. Chem. Chem. Phys.* **2019**, *21*, 12881.

[41] W. V. Gaens, A. Bogaerts, *Plasma Sources Sci. Technol.* **2014**, *23*, 35015.

[42] S. Norberg, Ph.D. Thesis. University of Michigan; 2015. https://deepblue.lib.umich.edu/handle/2027.42/113342. Accessed December 13, 2019.

[43] A. M. Lietz, M. J. Kushner, *J. Phys. D: Appl. Phys.* **2016**, *49*, 425204 [Corrigendum: J. Phys. D 50, 119501 (2017)].

[44] M. Teschke, J. Kedzierski, E. G. Finantu-Dinu, D. Korzec, J. Engemann, *IEEE Trans. Plasma Sci.* **2005**, *33*, 310.

[45] H. Motomura, H. Matsuba, M. Kawata, M. Jinno, *Jpn. J. Appl. Phys.* **2007**, *46*, L939.

[46] E. Karakas, M. A. Akman, M. Laroussi, *Plasma Sources Sci. Technol.* **2012**, *21*, 34016.

[47] F. A. Villamena, *Molecular Basis of Oxidative Stress*, John Wiley & Sons, Ltd., **2013**, pp. 1–48.

[48] C. C. Winterbourn, *Nat. Chem. Biol.* **2008**, *4*, 278.

[49] D. Gardoni, A. Vailati, R. Canziani, *Ozone Sci. Eng.* **2012**, *34*, 233.